Journal of Magnetic Resonance 323 (2021) 106879

Contents lists available at ScienceDirect

Journal of Magnetic Resonance

journal homepage: www.elsevier.com/locate/jmr

An integrated magnetic resonance plant imager for mobile use in greenhouse and field

Marco Meixner [a,b], Johannes Kochs [b], Petra Foerst [a], Carel W. Windt [b,*]

[a] Technical University Munich, SVT, Gregor-Mendel-Straße 4, 85354 Freising, Germany
[b] Forschungszentrum Jülich, IBG-2, Wilhelm-Johnen-Straße, Jülich, Germany

ARTICLE INFO

Article history:
Received 24 July 2020
Revised 5 November 2020
Accepted 24 November 2020
Available online 27 November 2020

Keywords:
MRI
Mobile
Portable
Small-scale
Low-field
Plants
In situ

ABSTRACT

In this contribution we demonstrate a mobile, integrated MR plant imager that can be handled by one single person and used in the field. Key to the construction of it was a small and lightweight gradient amplifier, specifically tailored to our combination of magnet, gradient coils and the requirements of the desired pulse sequences.

To allow imaging of branches and stems, an open C-shaped permanent magnet was used. In the design of the magnet, pole gap width, low weight and robustness were prioritized over homogeneity and field strength. To overcome the adverse effects of short T_2^*, multi-spin echo imaging was employed, using short echo times and high spectral widths. To achieve microscopic resolution under these constraints requires fast switching field gradients, driven by strong and fast gradient amplifiers. While small-scale spectrometers and RF amplifiers are readily available, appropriate small-scale gradient amplifiers or designs thereof currently are not. We thus constructed a small, 3-channel gradient amplifier on the basis of a conventional current-controlled AB amplifier design, using cheap and well-known parts. The finished device weighs 5 kg and is capable of delivering 40 A gradient pulses of >6 ms in duration.

With all components built onto an aluminum hand trolley, the imaging setup weighs 45 kg and is small enough to fit into a car. We demonstrate the mobility and utility of the device imaging quantitative water content and T_2, first of an apple tree in an orchard; second, of a beech tree during spring leaf flushing in a greenhouse. The latter experiment ran for a continuous period of 62 days, acquiring more than 6000 images.

1. Introduction

The development of mobile imagers and the application of mobile, field going NMR for use in plant science has long occupied the imagination of researchers [1–3], but has recently become more feasible than ever. Many components for small scale imagers have now become available, either in the form of published designs, or as ready-made commercial devices. This ranges from designs for small-scale and open (or openable) NMR magnets [4–8], via designs for small-scale, fully integrated or open source spectrometers [9–11], to examples for methods to design gradients for plane parallel magnets [12–14]. One of the most extensive studies describing the construction of a small-scale imager is that by Cooley et al. (2020) [15], who presented an affordable open source tabletop imager for teaching and testing purposes. They present details on the construction of all components of their imager, including the software and GUI.

Despite the availability of components that would lend themselves for the construction of mobile imagers, currently no devices appear to exist that are truly mobile. Efforts to explore the utility of MR imaging of trees in the open air so far all utilized one or more conventional, full sized components [16,17]. In one case these were made transportable by mounting the setup on an electric trolley [18]. To this date, the most mobile imager that has been presented was also one of the first [2]. It was based on a commercially available small-scale TD-NMR setup, coupled with a custom-made probe head, gradient coils and gradient amplifiers. The system was used to demonstrate imaging of plants in a greenhouse. It, however, still consisted of a number of loose, interconnected components and thus did not appear suitable to be moved around.

In this work we seek to construct a truly mobile MR imager that is tailored for imaging plants at microscopic resolutions, while remaining affordable and relatively easy to build. To be called mobile, we propose that an imager a) should consist of a single,

* Corresponding author.
E-mail address: c.windt@fz-juelich.de (C.W. Windt).

https://doi.org/10.1016/j.jmr.2020.106879
1090-7807/

integrated unit; b) should be light and mobile enough to be moved and handled by a single person; c) should be compact enough to fit in a regular sized car; and d) needs to be able to cope with the rigors of imaging in environments with large temperature variations and transport shocks.

In a previous study we constructed a magnet in which weight and size, as well as robustness and accessibility was prioritized over sheer magnet homogeneity [19]. The resulting C-shaped magnet has a total weight of 16 kg and can easily be re-shimmed mechanically to optimize the homogeneity of the magnetic field. It is fitted with custom-built, plane parallel gradient coils that are open from the front, yet strong and fast enough to enable the use of MSE-type sequences. The approach thus relied on a robust gradient set and a fast and powerful gradient amplifier. This requirement was easily met by a set of conventional gradient amplifiers, which, however, weighed more than 100 kg in total, making the setup large and cumbersome to move.

An integrated, truly mobile plant imager, utilizing this magnet and gradient set, would require a gradient amplifier of comparable power and speed, which at the same time would have to be small, light and robust. Unfortunately, devices of this kind have not been presented yet. Existing examples of custom-made devices are either not sufficiently mobile [16] or not sufficiently powerful [2,15]. Therefore, we here present a dedicated mobile gradient amplifier that is light and small, but at the same time sufficiently powerful to support MSE imaging at short echo times.

Using this amplifier, we constructed a practical, fully integrated mobile imager, designed specifically for imaging intact trees and plants in situ. The finished device has a total weight of 45 kg and is installed on a hand trolley. It can be moved across soft and uneven ground by a single person and allows imaging of plant organs at various heights and orientations. The mobility and functionality of the device in the field was demonstrated imaging an apple tree in an orchard. Its long-term stability was shown in a two-month greenhouse experiment, imaging the dynamics of dormancy release in the stem of a beech tree during and after spring leaf flushing.

2. Materials and methods

2.1. Mobile gradient amplifier: Design and construction

To be suitable for our purposes the gradient amplifier should allow for fast switching (<150 μs) and high current output (≥40 A). These are not requirements typically associated with small-scale, mobile amplifiers. Yet, they are needed to allow for short echo times, pulsed field gradient (PFG) flow measurements of xylem and phloem sap flow in plants (future application), as well as for imaging small objects with microscopic resolution at high spectral widths. So far, we employed a stack of conventional AB power amplifiers (BAFPA40, Bruker, Rheinstetten, Germany) to achieve these requirements and drive our gradients [19]. This set of gradient amplifiers weighed approximately 105 kg, and was mounted in a 19″ rack (height of 3 × 4RU or 3 × 178 mm). In the current work we set out to replace this set of amplifiers with a unit of much lower weight (<10 kg) and bulk. This set of small-scale amplifiers should allow mobile and optionally battery driven use in the greenhouse and field, but without sacrificing current output and slew rate.

As a basis for the power stage of the mobile amplifier we chose the well-established design for a conventional AB type audio amplifier published by Giesberts (1993) [21]. This design uses cheap, well-known parts, is easy to repair, and has a low resistance power stage. To approximate the maximum current and slew rate of the full-sized amplifiers in a mobile, small-scale AB-type amplifier, its efficiency needs to be much better than that of its full-sized counterpart. To achieve this goal, it is key to tailor the specifications of the amplifier to our plane parallel gradients. Due to their small size (diameter 60 mm), optimized design, thick 105 μm copper windings and low number of turns (4 in X and Y, 12 in Z) these gradients have an exceptionally low resistance (0.29 Ω in X and Y, 0.55 Ω in Z) and inductance. This allows fast slew rates even with low voltage amplifier output. Whereas the BAFPA40 reference amplifiers have a maximum output voltage of 120 V, we empirically found that 18 V already suffice to achieve a current of 40 A with a ramp time of 150 μs in the Z channel. Designing for lower output voltages markedly improves amplifier efficiency, as the average power loss (P_{loss}) at the transistors of the power stage (MOSFETS) scales with voltage:

$$P_{loss} = 1/T \int_0^T (I_{DS}(t) \cdot U_{DS}(t))dt$$

Here T represents time, I_{DS} drain-source current, and U_{DS} drain-source in-phase voltage. The maximum value of U_{DS} equals the supply voltage. By reducing the voltage of the power stages to the minimum value required by the gradient coils to achieve the desired slew rate, the heat loss per cycle in the MOSFETS was minimized. This voltage reduction also enables the use of smaller MOSFETS with a lower maximum voltage and therefore a lower internal resistance, resulting in again lower energy losses. However, there is a trade-off: the gains in efficiency come at the cost of flexibility. The amplifiers lose the ability to drive larger coils of higher impedance and will suffer a reduction in the duty cycle that can be supported.

The power stage [21] of the mobile amplifier was realized using MOSFETs IRF9540N and IRF540N in a TO-220 case (datasheet PD-91437B and PD-91341A). To increase maximum peak current and to decrease resistance we added a second pair of MOSFETs in parallel in the main branches, as simulated by Heinemann et al. [22] (Fig. 1b). No symmetrizing resistors for the current distribution were added, as would normally be used in this amplifier design. This resulted in a theoretical $R_{DS(on)}$ of 60 mΩ. The MOSFETS are cooled by means of a large aluminum cooling body and radial cooling fans (Fig. 2c, d). The cutoff frequency was 20 kHz. A standard current regulation was added as described by Cooley et al. [15], using a 50 mΩ shunt resistor as a compromise between accuracy and voltage drop.

Originally, the amplifier design mentioned above was meant to drive loads between 3 and 8 Ω. The much lower resistance of the gradient coils, in combination with parasitic inductances in the circuit, are likely to cause high peak voltages and oscillations that will damage the MOSFETS of the power stage. These oscillations were suppressed by empirically adding small capacitors between the base and collector of those transistors and in the current mirror circuit (marked *** in Fig. 1b). These additions did not increase pulse rise time.

Three gradient amplifiers were built on modular boards, designed to fit a lightweight 19″, 3RU modular euro chassis. One half of the chassis was taken up by the three gradient amplifiers, the other half of the chassis housed a set of two switched 24 V, 4 A power supplies (LS100-24, TDK-Lambda Americas Inc., Tokyo, Japan), weighing 0.6 kg each (Fig. 2). The dimensions of the power supplies (10 × 4 × 25 cm^3) are close to those of a set of heavy duty 25.9 V, 12,600 mAh lithium ion battery packs, weighing 2.0 kg each (PR-CU-R281, AA Portable power, Richmond, USA), which can easily be used to replace the power supplies, and allow for up to 8 h of continuous standalone use. Protection of gradient coils and amplifiers is ensured by fuses, as well as an analog timing circuit, limiting maximum pulse length, but allowing a shim current of

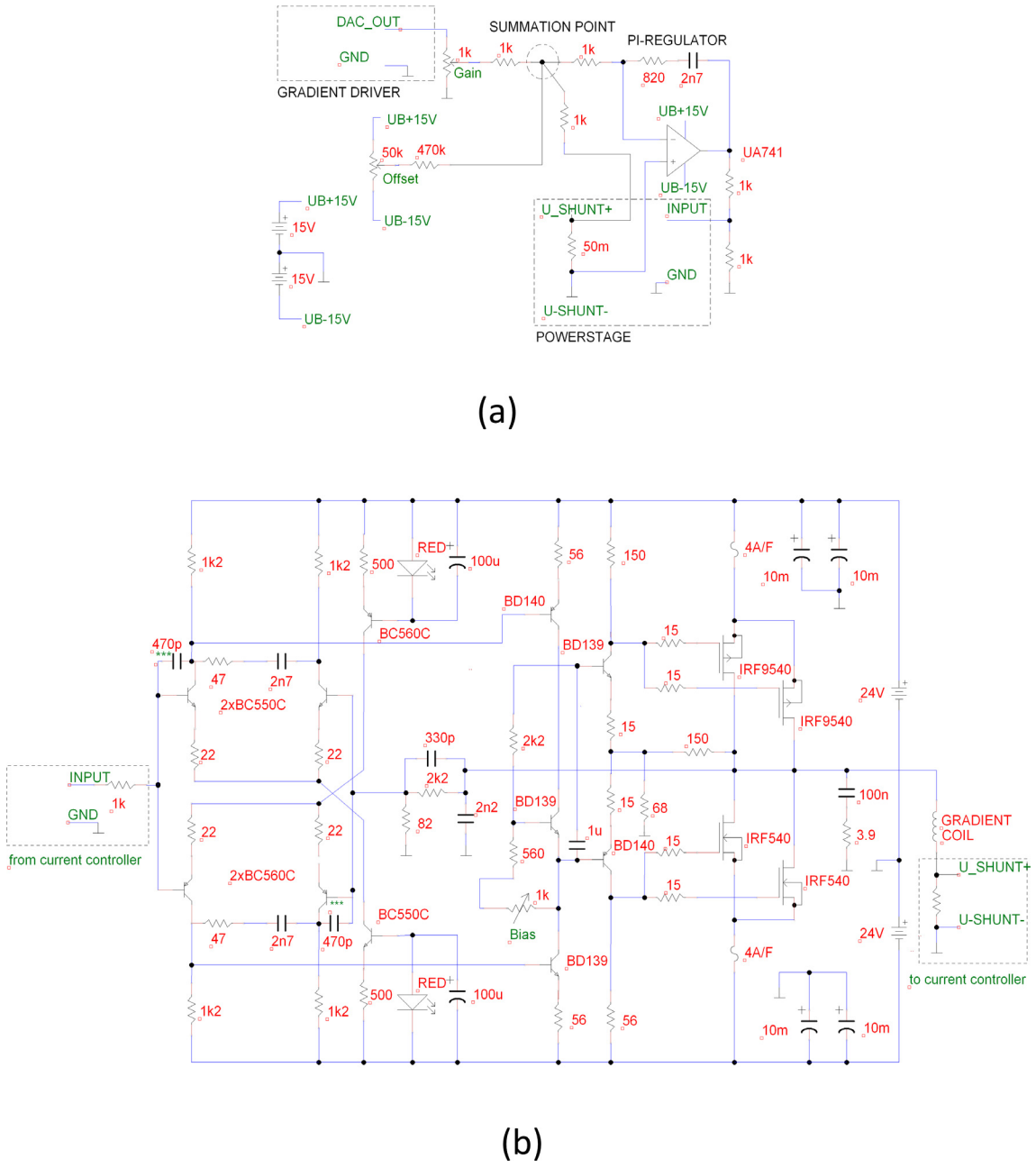

Fig. 1. Circuit diagrams of one channel of the small-scale AB gradient amplifier. The main components of the amplifiers were a pre-amplification circuit, a driver circuit, an operational amplifier based PI current regulator (shunt resistors voltage as feedback) and a power stage (MOSFET transistors 2 × IRF540, 2 × IRF9540 with a peak current >70A) (a). The power stage was based on a design published by Giesberts (1993) [21], to which capacitors were added for suppressing high peak voltages and oscillations, indicated by *** (b). To prevent voltage drop during pulsing, the supply lines of the three gradient boards were interlinked via the back plane resulting in a total capacity of 60,000 μF (not shown).

up to 2 A. Additionally, heat sink temperature is monitored for over temperature and the power stage disabled at temperatures > 70 °C.

The finished three channel amplifier weighs 5.0 kg fitted with two switched power supplies, or 7.8 kg when fitted with lithium ion battery packs. It is able to provide 40 A at a maximum voltage of 18 V per channel, for gradient pulses of up to 6 ms in duration, without significant current drop. The output current of the gradient amplifier as a function of the voltage, supplied by the gradient driver of the spectrometer, was shown to be linear (Fig. 3a). Driving the X gradient, not more than 9.5 V were required to achieve a current of 30 A with a rise time of 100 μs (Fig. 3b). In practical use, running MSE sequences at high resolution, care needed to be taken not to acquire too many echoes (<40 when measuring less than an hour, <25 during continuous imaging). At values beyond that the transistor junction of the read channel had a tendency to overheat, and the transistors needed to be replaced. This, however, was a cheap repair of little effort. Imaging with short echo times, the modest number of echoes that can be acquired will limit the accuracy of T_2 fitting when dealing with samples with a very long T_2 (>200 ms). This may for example be encountered in the large parenchymatic cells in the pith of herbaceous plants.

2.2. Magnet and probe head

A 0.25 T, 16 kg C-shaped permanent NdFeB magnet with a 40 mm air gap was custom-built and fit with a three-axis plane parallel gradient set with a maximum gradient strength of 0.3 T/m over a spherical volume of 25 mm in diameter in X and Y

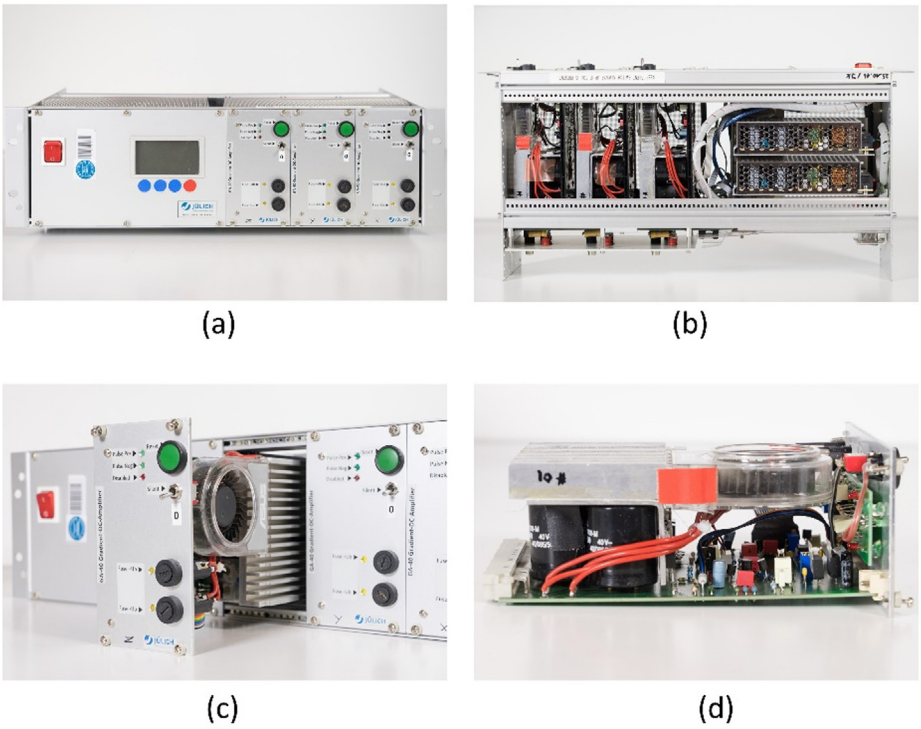

Fig. 2. Completed small-scale gradient amplifier. The front view (a) and top view with the cover removed (b) show the three amplifier modules (right in panel a), next to the power supply (left in panel a). The modular amplifier boards could be pulled out individually (c). The main transistors are fitted with an aluminum heat sink with a radial fan (d).

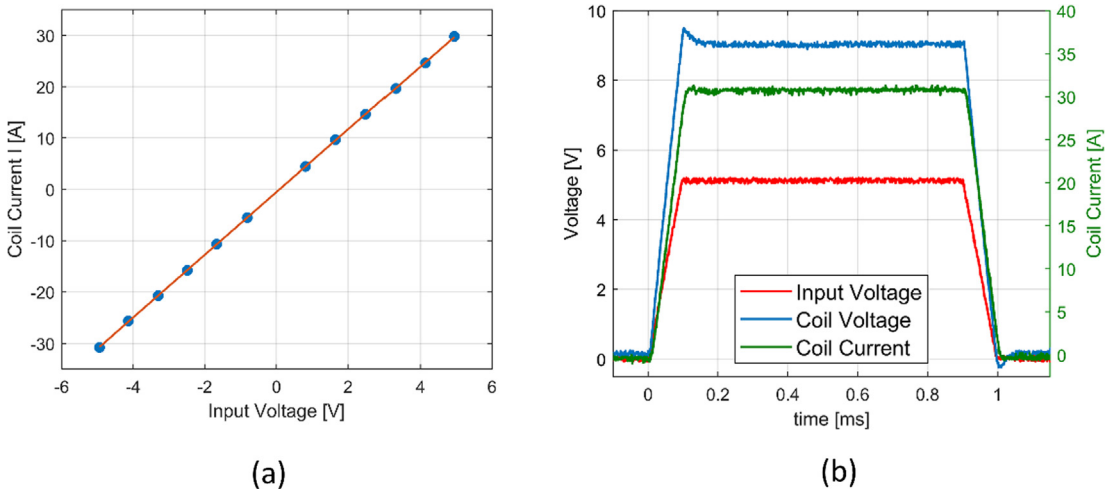

Fig. 3. Plot of the linearity of the output current of the gradient amplifier as a function of gradient driver voltage (a). Response curve of the amplifier during a 1 ms (100 µs rise time), 30 A pulse, connected to the X gradient (b). Amplifier input voltage is shown in red, coil voltage in blue and coil current in green. Current was monitored measuring the voltage drop over an additional 100 mΩ resistor mounted in series. (For interpretation of the references to color in this figure legend, the reader is referred to the web version of this article.)

direction. The diameter of the gradient coil set is 60 mm, the resistance 0.29 Ω for X and Y, and 0.55 Ω for the Z gradient. The gradient efficiency is 6.1 mT/m/A for X and Y and 22.3 mT/m/A for Z. The gradient plates were constructed on the basis of two-sided 105 µm copper circuit boards (OCTAMEX, London, United Kingdom). The gradient plates are mounted on an openable, aluminum frame that also serves as a Faraday cage (Fig. 4b). The openable probe head (RF coil, gradient coils and aluminum frame) can be rotated relative to the poles of the magnet to fit the orientation of the plant (Fig. 4c). RF coils on Teflon formers of an inner diameter of 10, 12.5, 15, 17.5 and 20 mm can be mounted in the probe head (Fig. 4d). The solenoidal coils are hand-wound onto the split Teflon formers. To reduce magnetic field drift due to temperature changes, the poles of the magnet are equipped with resistive heating wire, coupled to an accurate temperature controller (±0.1 K regulation error) that regulated magnet temperature to a set point approximately 5 °C above ambient temperature. Further details on the magnet and probe head are given in Meixner et al. [19].

2.3. Mobile MRI hand trolley

A custom-made aluminum hand trolley with large air-filled tires was constructed as a carrier for the MR imager. A sturdy aluminum pole, that was welded to the trolley frame, supports the

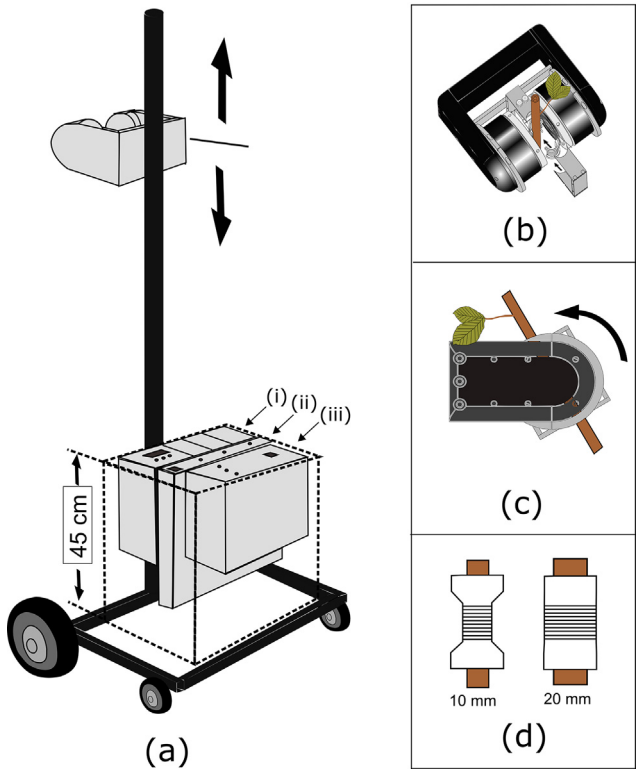

Fig. 4. Sketch of the mobile magnetic resonance imager. The setup was assembled onto a lightweight aluminum hand trolley (a). A C-shaped permanent magnet was mounted on a sturdy aluminum pole that was fixed to the hand trolley. The magnet can be moved up and down on the pole (max. height of 160 cm). The electronic components comprise a custom-built, small-scale, 3-axis gradient amplifier (i), a pre-emphasis unit (ii), and a Kea II spectrometer with built-in RF amplifier (iii). The probe head and RF coil can be opened, allowing plant stems or branches to be inserted (b). The angle of the probe head can be adjusted relative to the magnet to match the angle of the object of interest (c). The diameter of the split Teflon former of the RF coil can be chosen to closely match the diameter of the plant shoot (10–20 mm) (d).

magnet; the magnet is fixed relative to the pole with two quick release clamps. The pole provides a convenient handle to recline the trolley onto its large rear tires and move the trolley around. After parking, the magnet can be slid up the pole for easy mounting at heights between 50 and 160 cm. During the orchard measurement the magnet was covered with a thin sheet of flexible insulation foam, shielding it from the low ambient temperature (7 °C). Included in the imaging setup are the 3-axis gradient amplifier, a Kea II spectrometer (Magritek, Wellington, New Zealand) with a standard built-in 100 W RF amplifier, and a pre-emphasis unit (Resonance Research, Billerica, USA). The imaging console is operated with a standard laptop, running the proprietary spectrometer software Prospa V3.21 (Magritek, Wellington, New Zealand). The electronic components of the imager are mounted side by side in a 19″ rack at the bottom of the trolley, lowering the center of gravity and countering the weight of the magnet on the pole (Fig. 4a). The entire imager (trolley, magnet and electronic components) weighs 45 kg.

2.4. Plant material, treatment and handling

Two demonstrator experiments are presented in this contribution. The first one was conducted on a full-grown commercial apple tree (Malus domestica cv. Captan), grown in the open air in an orchard at the Research Campus Klein-Altendorf, Rheinbach, Germany. Here, the magnet was mounted on a branch with a diameter of 10 mm at a height of about 1.5 m (Fig. 5).

The second demonstrator measurement was a long-term experiment during which the dormancy release (spring awakening) of a 150 cm tall beech tree (*Fagus sylvatica*) was monitored. The tree was purchased in mid-winter from a local nursery (Baumschule Leonhard Veith, Merzenich-Golzheim, Germany). Prior to the experiment the plant was grown in the open air, at temperatures between −7 and 5 °C. At the end of winter dormancy release was forced by moving the tree into the greenhouse, exposing it to long day length and higher temperatures (20 °C, 16 h day; 16 °C, 8 h night; 250 μmol m^2 s^{-1} PAR in supplemental lighting by metal halogen vapor lamps (250 W SON-Agro, Philips, Eindhoven, the Netherlands)). At the measurement position, 135 cm above the soil, the stem had a diameter of 18 mm. Imaging was started directly after moving the plant to the greenhouse. For this long-term measurement any movement of the plant relative to the imager was avoided by minimizing tension in the branch due to its fixation, as the gradual release of such tensions by tree growth was found to cause movement and potential ghosting artefacts in prior experiments.

2.5. MR Imaging, parameters and processing

The following steps were performed prior to image acquisition: (i) Adjustment the height of the magnet and the angle of the probe head to match that of the branch; (ii) winding the coil around the shoot; (iii) sliding the branch with the coil into the probe head; closing of the probe head and covering it with an earthed silver-plated copper mesh, (iv) tuning and matching of the coil, finding pulse settings and (v) optimizing the angle of the probe head so that it is perfectly perpendicular to the branch. The latter was done by imaging side projections of the shoot. Small adjustments of the position and angle of the branch were done by means of aluminum clamps, fastened onto the MRI hand trolley above and below the position of the magnet. All image acquisition was done with an MSE imaging pulse sequence as described by Edzes et al. [20], employing an XY-8 phase cycling scheme [19,23].

For the orchard experiment a 15 mm diameter solenoidal coil was employed. Images at two matrix sizes were acquired, 128 × 128 and 64 × 64, both with a field of view (FOV) of 16.7 × 16.7 mm, a slice thickness of 4 mm and the following settings: Slice selective 90° pulse: 500 μs soft five lobe sinc, −38 dB; hard 180° pulses: 7.8 μs, −16 dB; 40 echoes; echo time (TE) 4 ms, spectral width (SW) 100 kHz. Images with a matrix size of 64 × 64 were acquired with a repetition time (TR) of 2.5 s and 4 averages, resulting in a total image acquisition time of 5 min. The 128 × 128 images were acquired with a TR of 1.5 s and 16 averages, resulting in an image acquisition time of 50 min. The ambient temperature during the measurement was around 7 °C; the magnet set point temperature was 12 °C.

For the long-term dormancy release experiment a 20 mm diameter solenoidal coil was employed. In the greenhouse the tree was imaged continuously for 62 days until its leaves had fully emerged and the first leaves reached maturity. Imaging was done every 15 min, with the following settings: matrix size 128 × 128, FOV 24 × 24 mm, slice thickness 5 mm, 4 averages, TR 1.5 s, TE 5 ms, 24 echoes, 90° pulse: −36.5 dB, 500 μs five lobe sinc; hard 180° pulses: −16 dB, 9.9 μs; SW of 100 kHz. Despite the active temperature control of the magnet, strong temperature changes in the greenhouse or direct solar irradiation caused small changes in B_0. To compensate, resonance frequency was automatically determined between measurements and B_1 frequency adjusted to match.

Passive and active shimming of the magnet was done once, directly after mounting the tree into the imager. Subsequently

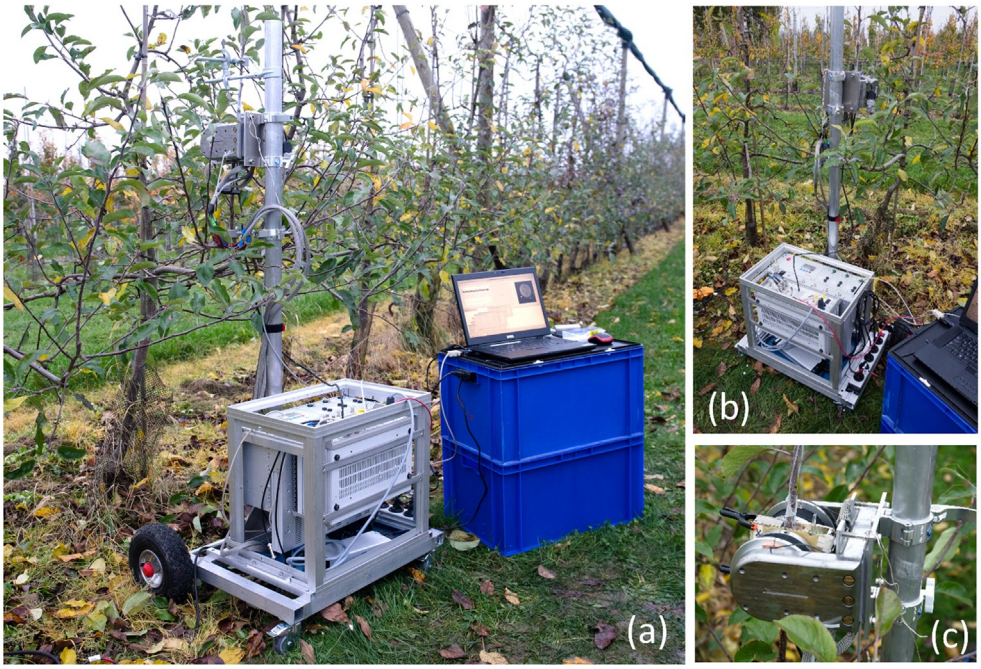

Fig. 5. The mobile MRI scanner in an orchard (Research Campus Klein-Altendorf, Rheinbach, Germany) (a). The imaging hardware was installed onto a 19″ frame, mounted on an aluminum hand trolley. The C-shaped permanent magnet was supported by an aluminum pole, which was an integral part of the hand trolley (c). By sliding up or down the magnet was adjusted in height. Empty plastic crates (blue) provided a makeshift table for the laptop. (For interpretation of the references to color in this figure legend, the reader is referred to the web version of this article.)

active shimming was done and checked every two weeks, but no significant adjustments were needed during the entire 62 day period.

All image acquisition and data processing was programmed in Prospa (Magritek, Wellington, New Zealand). First, all images were masked and phase corrected according to Ma (2008) [24]. Quantitative water content (A) and T_2-maps were calculated on the basis of a mono-exponential fit of the signal for every pixel. In the dormancy release experiment, all water content maps were normalized on the basis of the reference tube. A*T_2 product maps were obtained by performing a pixel-by-pixel multiplication of the amplitude- and T_2-maps [19]. A*T_2 product maps were shown to be especially helpful to visualize filled xylem vessels in trees. Xylem vessels tend to be smaller than can be spatially resolved, but give rise to pixels with elevated water content (A) and T_2. By multiplying the two parameter maps, the contrast between wood with and without filled xylem vessels is greatly enhanced, enabling the detection of pixels with filled xylem vessels even less than half the cross sectional area of those pixels is occupied by xylem sap [19]. In the greenhouse experiment, before T_2-fitting, all images were calculated based on sliding window averaging of 36 MSE measurements. To filter out noise in the animations of sequential images, pixels with values that were double or more, or half or less, than all four nearest neighboring pixels were assumed to be noise and set to zero (supplementary Fig. S1 and S2).

3. Results and discussion

3.1. Orchard field-measurement

The mobility and robust nature of the mobile MRI scanner were demonstrated by imaging the branch of an apple tree (Malus domestica cv. Captan) in a research orchard (Fig. 5). The experiment was done in early November on a day with a maximum temperature of 7 °C. The device was loaded into the trunk of a car and taken to the measurement site. Thanks to the large air-filled tires the device could be wheeled with ease from the car to the tree of choice by a single person, unhindered by the soft and uneven field. After adjusting the set point of the temperature controller of the magnet to approximately 12 °C, magnet temperature equilibrated within about two hours. Prior to taking the setup out of the lab, the magnet was at a set point temperature of approximately 25 °C. In the car magnet temperature was not controlled and ambient temperature was approximately 20 °C. The robust and basic construction of the magnet allowed re-shimming it in minutes at the site of measurement, correcting for the potential effects of transport shocks and temperature changes. Passive shimming was done by adjusting the pole shoe alignment of the magnet; active shimming was done by means of the three gradient coils.

Images of the branch were obtained at two matrix sizes (64×64 and 128×128), both with the same FOV (16.7×16.7 mm). At a matrix size of 64×64 a full dataset could be acquired within 5 min, from which water content and T_2 images with a pixel size of 0.26×0.26 mm were obtained. At a matrix size of 128×128 (pixel size 0.13×0.13 mm) image acquisition took 50 min. During this time, no artefacts (such as blurring or image deformation) were observed, indicating that the magnet temperature was held sufficiently constant to prevent temperature induced shifts of B_0 (Fig. 6).

Images readily allowed to differentiate stem tissues, such as bark (water content 30%, T_2 40 ms), cambium (water content 50%, T_2 80 ms), xylem (water content 30 to 40%, T_2 70 to 100 ms) and pith (water content 55%, T_2 145 ms). The uniform water content (A) and T_2 values of the xylem reflected the homogeneous vessel distribution in the wood, as observed by light microscopy after harvesting (not shown). In amplitude (64×64: 0.107, 128×128: 0.115) and T_2 (64×64: 81.2 ms, 128×128: 74.9 ms) the average values of images acquired with both matrix sizes agreed within an error range <10% (Fig. 6).

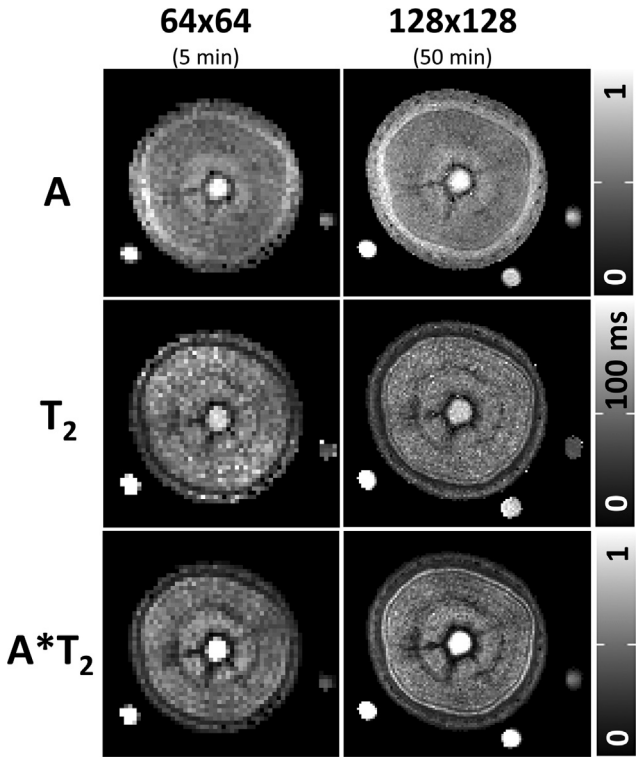

Fig. 6. Amplitude (A), T_2, A^*T_2 images of an apple branch, acquired with the mobile imager in an orchard. Field of view 16.7 × 16.7 mm. At a matrix size of 64 × 64 (left column) image acquisition took 5 min, at a matrix size of 128 × 128 (right column) 50 min.

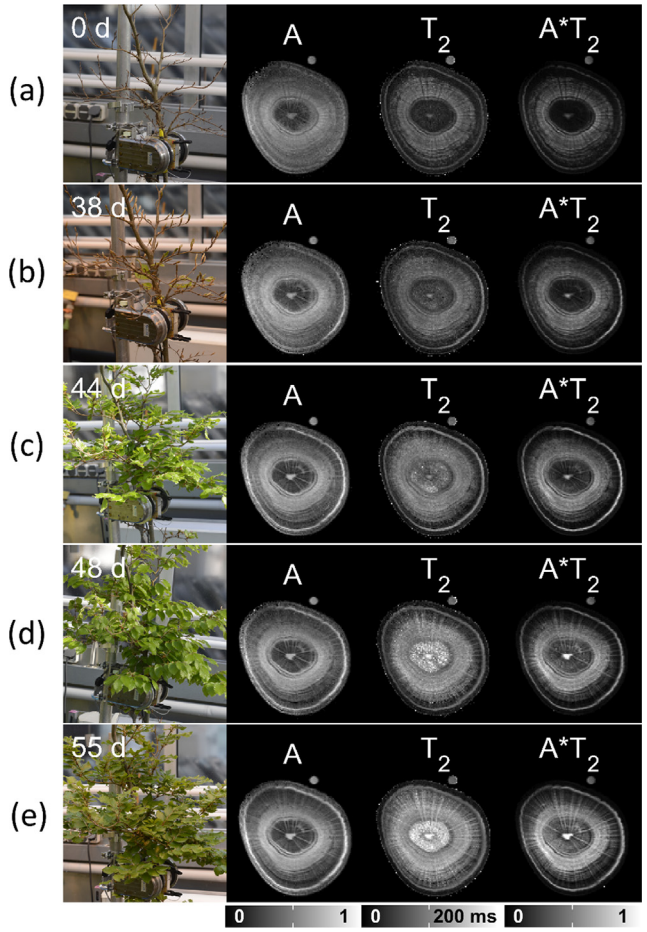

Fig. 7. Long-term greenhouse experiment, monitoring the stem of a beech tree (*Fagus sylvatica*) during bud flushing, leaf development and leaf maturation. The tree was imaged continuously for a period of 62 days; shown are images acquired between day 0 (a) – day 55 (e). Every MRI parameter map represents the sliding window average of 36 measurements, acquired over a period of 9 h. A photo of the branches of the tree is shown next to the corresponding amplitude (A), relaxation time (T_2) and A^*T_2 product images. An animation of the whole 62 day experiment is provided as supplementary material (S1).

3.2. Long-term greenhouse measurement

As a demonstrator experiment for the long term use of the imager in an agronomical setting with strongly varying environmental conditions, the MRI scanner was set up in a greenhouse to monitor an 18 mm diameter beech stem (*Fagus sylvatica*) during bud burst and leaf flushing, for a continuous period of 62 days (Fig. 7). In the greenhouse the imager experienced diurnal temperature changes between 18 and 28 °C and was occasionally exposed to direct sunlight and high air humidity. During the experimental period B_0 showed a variation of 9.8 kHz at the very extremes, but usually did not show a diurnal drift of more than 3.9 kHz (Fig. S3), i.e. half a pixel at a matrix size of 128 at a spectral width of 100 kHz. This was easily corrected by determining and adjusting resonance frequency between measurements. The imager remained functional for the whole time, acquiring>6000 images sequentially, demonstrating the reliability and durability of the setup in the challenging greenhouse environment.

The water content and T_2 values of the various tissues in the stem (bark, cambium and phloem, xylem, pith; Fig. 7) were in line with previous experiments imaging beech [19,25]. In the xylem, one large and mostly connected ring of tissue had the highest water contents (33 to 40%) and T_2 values (50 to 90 ms). Over a period of 62 days, water content in this ring increased from around 35% to values of up to 57%; while T_2 increased from around 70 ms to a maximum value of 127 ms. In the oldest xylem in the center, T_2 increased from 30 ms to more than 100 ms, while water content values in this area increased from 15 to 20% (Fig. 7).

The average water content and T_2 values of the stem were found to oscillate diurnally during the whole experiment (Fig. 8a). Both parameters exhibited fluctuations of around 3 to 4%, with a maximum in the morning and a minimum in the evening. Both quantities thus reflect the diurnal pattern of the depletion of stem water reserves during the day and their replenishment during the night [1,7,8,26,27]. The diurnal pattern of fluctuation closely matched that which is observed when measuring stem diameter variations by means of dendrometers [5,28]. In vivo MRI of oak revealed that most of the diurnal shrinkage and swelling in that species is caused by water content fluctuations in the elastic bark tissues [27]. The water content fluctuations that we observed in the bark after leaf emergence (supplementary animations S2c and S2d) mirror this behavior and suggest that the same holds true in beech.

Bud development during the first 36 days, prior to leaf emergence, coincided with a moderate increase in stem water content (~10%; Fig. 8b-c). This increase was observed mainly in the bright xylem ring. Between day 0 and 20 the average T_2 value of the stem increased from 47 to 63 ms. This became visible throughout the xylem, but was especially noticeable in the older year rings (Fig. 8b). Between days 20 to 37 the stem average T_2 value went back down to 53 ms, with T_2 decreasing again throughout the xylem (Fig. 8a, c). Between day 37 and 47 the first leaves emerged, while a significant T_2 increase in the older xylem and the pith was observed (Fig. 8d). The rays stood out in T_2 and A^*T_2 images, while a more moderate T_2 increase was observed in the younger xylem. Between day 47 and day 61 water content increased significantly in the cambium and in the younger xylem, resulting in an average

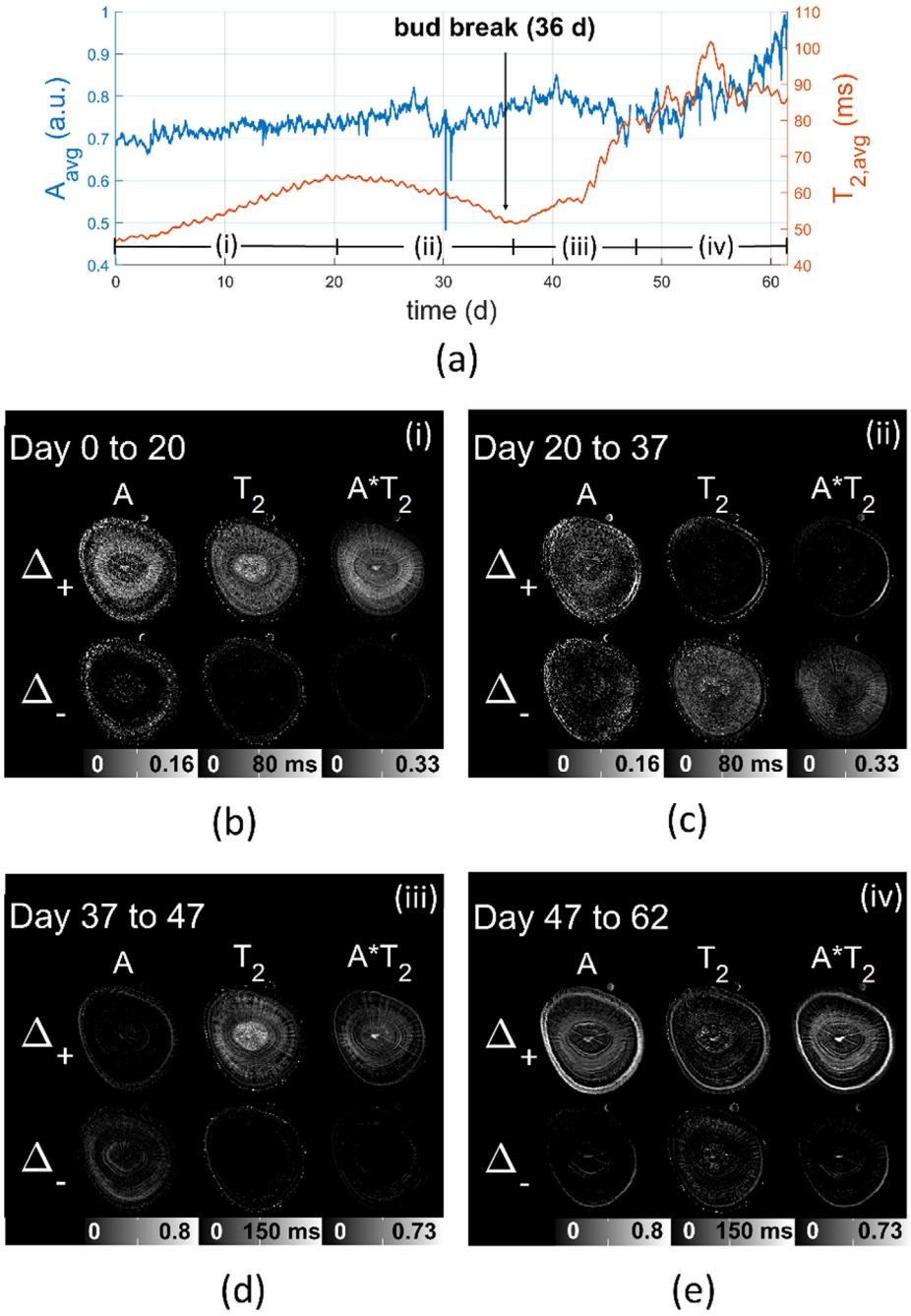

Fig. 8. Average amplitude (A), T_2, and A^*T_2 in the stem of beech during bud flushing and leaf maturation over a period of 62 days (a). The most significant positive and negative changes during periods (i) to (iv) in the A, T_2 and A^*T_2 parameter maps are shown in panels b-e. Positive changes in the respective time periods are shown in the top half of the panels (Δ_+), negative changes in the bottom half (Δ_-). The scaling of the water content and A^*T_2 product images is relative to the scaling used in Fig. 6. Animations representing the timeframes of panel b) - e) are provided as supplementary material (S2a-d).

water content increase of 36% (Fig. 8a, e). This was accompanied by a moderate change in T_2 in the cambium.

The observed T_2 of water in compartments in porous structures such as plant tissues is negatively correlated with compartment size if, after excitation, magnetization bearing protons are likely to reach the compartment wall by diffusion in a timescale shorter than the intrinsic (or bulk) T_2 of the liquid [29]. This correlation has been observed for living vacuolated plant tissues [30,31], as well as for woody xylem conduits [32,33]. In the context of drought stress in trees, we utilized this effect to monitor embolism formation (i.e, the collapse of water columns) in xylem conduits [19]. In the context of flushing, an increase in T_2 as observed in Fig. 8b and d may reflect the swelling of compartments, or water entering larger, previously empty lumina. Other factors that are associated with flushing and that might influence T_2, such as an increased sugar concentration in the xylem sap, or an increased membrane permeability, are unlikely to have caused the T_2 increase. They would both rather have caused the opposite effect, a decrease in the observed T_2 [34,35].

In temperate angiosperms including beech [36], a substantial part of the conductive xylem tissue is embolized due to freeze-thaw cycles during winter [37,38]. In beech, active refilling is the dominant mechanism to reestablish xylem function [39], allowing for flow resumption during leaf development [40]. Refilling is

thought to involve the wood rays, consisting of radially aligned files of specialized parenchyma cells. They form a link between xylem and phloem, and allow radial bi-directional transport of water and solutes. Rays were found to be involved in the storage and remobilization of starch, sugars, protein and fats [41,42]. Sucrose and other soluble sugars are essential for the development of new leaves in spring. They were found to arise from starch mobilization, after which they are radially translocated from the rays to the phloem, or the conduit lumen [43,44]. Tantalizingly, indirect evidence for both processes would appear to become visible in the increases in amplitude and T_2 of the rays (Fig. 8a, 8d, supplemental animation S2a, S2c, S2d) and in T_2 for the potential mobilization of starch in the center of the tree (Fig. 8d, supplemental animation S2c, from day 45 onwards).

Copini et al. [45] used MRI to monitor dormancy release in oak by imaging and subsequently harvesting two individuals per phenophase from April till June. Even though oak has a ring porous wood architecture that is different from semi-diffuse porous beech, similarities in the pattern of spring refilling were found. For both species, before bud break water in the stem was distributed fairly diffusely and homogeneously (Fig. 7a). Upon dormancy release average stem water content increased only moderately, but marked increases in water content were observed in the newly formed xylem (Fig. 8e). In both species water in the older year rings appeared to converge in particular regions, increasing contrast between wood regions with and without water. Copini et al. found the development of new vessels to coincide with leaf formation. In beech we also observed the start of xylem formation to coincide with bud break.

The T_2 dynamics between day 37 and 47 are particularly interesting (Fig. 8d). Bud break was accompanied by the start of a strong increase in the T_2 of the oldest xylem and the pith in the middle of the plant. Due to its low water content (~15%) this region would not appear to contain conducting xylem. The strong increase in T_2 in the center was accompanied by a more moderate T_2 increase in the surrounding xylem tissue, with especially the wood rays standing out (Fig. 8d). These increases in T_2 were followed between day 47 and 61 by a marked increase in water content in the cambium and the younger xylem, indicating radial growth (Fig. 8e, see supplementary animations S2c,d for details). This suggests that older xylem may have been used for storing starch. The increase in T_2 then may be associated with the mobilization (hydrolyzation) of starch into of soluble sugars around bud break. Such soluble sugars are osmotically active, attracting water and potentially causing a local increase in turgor. The sugars are subsequently transported via the rays to the xylem vessels, supporting xylem refilling and flow resumption, as well as to the cambium to support growth [46]. In spring, when sugars are mobilized, wood ray cells are likely to attract water and swell. The resulting decrease in surface-to-volume ratio may have caused the observed increase in the T_2 of the wood rays.

4. Conclusion

We presented a fully integrated, mobile plant imager with a maximum field of view of 20 mm.

To be able to run an MSE pulse sequence with short echo times and high spectral width, while achieving microscopic resolution, we constructed a small-scale gradient amplifier that was capable of generating pulses of up to 40 A at a duration of up to 6 ms.

By mounting all components of the MRI scanner (magnet, spectrometer, pre-emphasis unit, gradient amplifier) on a hand trolley, a mobile imager was obtained that could be moved by one person, transported in a regular car and used in the field. It was capable of delivering water content and T_2 images of high quality, while operating under challenging environmental conditions and over extended periods of time.

All components that were custom built for the imager (i.e., the magnet, gradient coils and gradient amplifier) were of well-known design and could potentially be manufactured at low to moderate cost, especially if produced in larger numbers. The spectrometer was the most expensive element in the imager. In the future, by also replacing the spectrometer with an affordable open source design, the imaging setup could become more affordable still. This, as well as the fact that the machine could easily be shared between labs, could make MRI available more widely for applications in plant physiology. Cheaper measurement time would also allow imaging of plants over extended periods of time.

Declaration of Competing Interest

The authors declare that they have no known competing financial interests or personal relationships that could have appeared to influence the work reported in this paper.

Acknowledgements

The authors acknowledge the financial support received from the German Research Foundation (DFG, grant number GRC81) through the TUM International Graduate School of Science and Engineering (IGSSE); and from the IBG-2: Plant Sciences institute at the Forschungszentrum Jülich. We thank Martina Tomasella for doing the microscopic image of the apple tree, Daniel Pflugfelder for his help with phase correction, and Dagmar van Dusschoten for various helpful discussions. We thank Michael Poole for the design of the gradient coils. Prof. Ulrich Schurr is gratefully acknowledged for making the presented research possible.

Appendix A. Supplementary data

Supplementary data to this article can be found online at https://doi.org/10.1016/j.jmr.2020.106879.

References

[1] H. Van As, J.E.A. Reinders, P.A. de Jager, P. van de Sanden, T.J. Schaafsma, In situ plant water balance studies using a portable NMR spectrometer, J. Exp. Bot. 45 (1994) 61–67, https://doi.org/10.1093/jxb/45.1.61.
[2] M. Rokitta, E. Rommel, U. Zimmermann, A. Haase, Portable nuclear magnetic resonance imaging system, Rev. Sci. Instrum. 71 (2000) 4257, https://doi.org/10.1063/1.1318922.
[3] B. Goodson, Mobilizing magnetic resonance, Phys. World 19 (2006) 28.
[4] T. Umebayashi, K. Fukuda, T. Haishi, R. Sotooka, S. Zuhair, K. Otsuki, The developmental process of xylem embolisms in pine wilt disease monitored by multipoint imaging using compact magnetic resonance imaging, Plant Physiol. 156 (2011) 943–951, https://doi.org/10.1104/pp.110.170282.
[5] C.W. Windt, P. Blümler, A portable NMR sensor to measure dynamic changes in the amount of water in living stems or fruit and its potential to measure sap flow, Tree Physiol. 35 (2015) 366–375, https://doi.org/10.1093/treephys/tpu105.
[6] K. Fukuda, D. Kawaguchi, T. Aihara, M.Y. Ogasa, N.H. Miki, T. Haishi, T. Umebayashi, Vulnerability to cavitation differs between current-year and older xylem: non-destructive observation with a compact magnetic resonance imaging system of two deciduous diffuse-porous species, Plant Cell Environ. 38 (2015) 2508–2518, https://doi.org/10.1111/pce.12510.
[7] C.W. Windt, H. Soltner, D. van Dusschoten, P. Blümler, A portable Halbach magnet that can be opened and closed without force: the NMR-CUFF, J. Magn. Reson. 208 (2011) 27–33, https://doi.org/10.1016/j.jmr.2010.09.020.
[8] S. Lechthaler, E.M.R. Robert, N. Tonné, A. Prusova, E. Gerkema, H. van As, N. Koedam, C.W. Windt, Rhizophoraceae mangrove saplings use hypocotyl and leaf water storage capacity to cope with soil water salinity changes, Front. Plant Sci. 7 (2016) 895, https://doi.org/10.3389/fpls.2016.00895.
[9] K. Takeda, OPENCORE NMR: open-source core modules for implementing an integrated FPGA-based NMR spectrometer, J. Magn. Reson. 192 (2008) 218–229, https://doi.org/10.1016/j.jmr.2008.02.019.
[10] C.A. Michal, A low-cost multi-channel software-defined radio-based NMR spectrometer and ultra-affordable digital pulse programmer, Concepts

Magnetic Reson. Part B: Magnetic Reson. Eng. 48 (2018) e21401, https://doi.org/10.1002/cmr.b.21401.
[11] J.B.W. Webber, P. Demin, Credit-card sized field and benchtop NMR relaxometers using field programmable gate arrays, Magn. Reson. Imaging 56 (2019) 45–51, https://doi.org/10.1016/j.mri.2018.09.018.
[12] W. Liu, D. Zu, X. Tang, H. Guo, Target-field method for MRI biplanar gradient coil design, J. Phys. D Appl. Phys. 40 (2007) 4418.
[13] M. Zhu, L. Xia, F. Liu, S. Crozier, Deformation-space method for the design of biplanar transverse gradient coils in open MRI systems, IEEE Trans. Magn. 44 (2008) 2035–2041, https://doi.org/10.1109/TMAG.2008.923898.
[14] Y. Wang, Q. Wang, L. Guo, Z. Chen, C. Niu, F. Liu, An actively shielded gradient coil design for use in planar MRI systems with limited space, Rev. Sci. Instrum. 89 (2018) 95110.
[15] C.Z. Cooley, J.P. Stockmann, T. Witzel, C. LaPierre, A. Mareyam, F. Jia, M. Zaitsev, Y. Wenhui, W. Zheng, P. Stang, Design and implementation of a low-cost, tabletop MRI scanner for education and research prototyping, J. Magnetic Resonance 310 (2020) 106625, https://doi.org/10.1016/j.jmr.2019.106625.
[16] M. Jones, P.S. Aptaker, J. Cox, B.A. Gardiner, P.J. McDonald, A transportable magnetic resonance imaging system for in situ measurements of living trees: The Tree Hugger, J. Magn. Reson. 218 (2012) 133–140, https://doi.org/10.1016/j.jmr.2012.02.019.
[17] A. Nagata, K. Kose, Y. Terada, Development of an outdoor MRI system for measuring flow in a living tree, J. Magn. Reson. 265 (2016) 129–138, https://doi.org/10.1016/j.jmr.2016.02.004.
[18] T. Kimura, Y. Geya, Y. Terada, K. Kose, T. Haishi, H. Gemma, Y. Sekozawa, Development of a mobile magnetic resonance imaging system for outdoor tree measurements, Rev. Sci. Instrum. 82 (2011) 53704, https://doi.org/10.1063/1.3589854.
[19] M. Meixner, M. Tomasella, P. Foerst, C.W. Windt, A small-scale MRI scanner and complementary imaging method to visualize and quantify xylem embolism formation, New Phytol. 33 (2020) 1502, https://doi.org/10.1111/nph.16442.
[20] H.T. Edzes, D. van Dusschoten, H. van As, Quantitative T2 imaging of plant tissues by means of multi-echo MRI microscopy, Magn. Reson. Imaging 16 (1998) 185–196, https://doi.org/10.1016/S0730-725X(97)00274-9.
[21] T. Giesberts, HEXFET-medium-power-amp: symmetrische FET-endstufe, ELEKTOR Magazine 12 (1993).
[22] R. Heinemann, Braunschweig, Germany, PSpice-Simulation eines 120 W Leistungsverstärkers mit komplementären MOSFets IRF150 und IRF9140, 2012. http://www.spicelab.de/mosfet_endstufe.htm (accessed 18 July 2019).
[23] C.W. Windt, F.J. Vergeldt, H. van As, Correlated displacement-T2 MRI by means of a pulsed field gradient-multi spin echo method, J. Magn. Reson. 185 (2007) 230–239, https://doi.org/10.1016/j.jmr.2006.12.015.
[24] J. Ma, Z. Slavens, W. Sun, E. Bayram, L. Estowski, K.-P. Hwang, J. Akao, A.T. Vu, Linear phase-error correction for improved water and fat separation in dual-echo dixon techniques, Magn. Reson. Med. 60 (2008) 1250–1255, https://doi.org/10.1002/mrm.21747.
[25] M. Merela, A. Sepe, P. Oven, I. Sersa, Three-dimensional in vivo magnetic resonance microscopy of beech (Fagus sylvatica L.) wood, MAGMA 18 (2005) 171–174, https://doi.org/10.1007/s10334-005-0109-5.
[26] K. Steppe, R. Lemeur, An experimental system for analysis of the dynamic sap-flow characteristics in young trees: Results of a beech tree, Functional Plant Biol. 31 (2004) 83–92, https://doi.org/10.1071/FP03150.
[27] V. de Schepper, D. van Dusschoten, P. Copini, S. Jahnke, K. Steppe, MRI links stem water content to stem diameter variations in transpiring trees, J. Exp. Bot. 63 (2012) 2645–2653, https://doi.org/10.1093/jxb/err445.
[28] P. Köcher, V. Horna, C. Leuschner, Stem water storage in five coexisting temperate broad-leaved tree species: significance, temporal dynamics and dependence on tree functional traits, Tree Physiol. 33 (2013) 817–832, https://doi.org/10.1093/treephys/tpt055.
[29] H. van As, Intact plant MRI for the study of cell water relations, membrane permeability, cell-to-cell and long distance water transport, J. Exp. Bot. 58 (2007) 743–756, https://doi.org/10.1093/jxb/erl157.
[30] L. van der Weerd, M.M.A.E. Claessens, T. Ruttink, F.J. Vergeldt, T.J. Schaafsma, H. van As, Quantitative NMR microscopy of osmotic stress responses in maize and pearl millet, J. Exp. Bot. 52 (2001) 2333–2343, https://doi.org/10.1093/jexbot/52.365.2333.
[31] L. van der Weerd, S.M. Melnikov, F.J. Vergeldt, E.G. Novikov, H. van As, Modelling of self-diffusion and relaxation time NMR in multicompartment systems with cylindrical geometry, J. Magn. Reson. 156 (2002) 213–221, https://doi.org/10.1006/jmre.2002.2550.
[32] N.M. Homan, C.W. Windt, F.J. Vergeldt, E. Gerkema, H. Van As, 0.7 and 3 T MRI and sap flow in intact trees: xylem and phloem in action, Appl. Magn. Reson. 32 (2007) 157–170, https://doi.org/10.1007/s00723-007-0014-3.
[33] Araujo, MacKay, Hailey, Whittall, Le, Proton magnetic resonance techniques for characterization of water in wood: application to white spruce, 1992.
[34] B.P. Hills, S.L. Duce, The influence of chemical and diffusive exchange on water proton transverse relaxation in plant tissues, Magn. Reson. Imaging 8 (1990) 321–331, https://doi.org/10.1016/0730-725X(90)90106-C.
[35] L. van der Weerd, M.M.A.E. Claessens, C. Efde, H. Van As, Nuclear magnetic resonanceimaging of membrane permeability changes in plants during osmoticstress, Plant Cell Environ 25 (2002) 1539–1549, https://doi.org/10.1046/j.1365-3040.2002.00934.x.
[36] M. Borghetti, S. Leonardi, A. Raschi, D. Snyderman, R. Tognetti, Ecotypic variation of xylem embolism, phenological traits, growth parameters and allozyme characteristics in Fagus sylvatica, Funct. Ecol. (1993) 713–720.
[37] J.S. Sperry, J.E.M. Sullivan, Xylem embolism in response to freeze-thaw cycles and water stress in ring-porous, diffuse-porous, and conifer species, Plant Physiol. 100 (1992) 605–613, https://doi.org/10.1104/pp.100.2.605.
[38] T. Améglio, C. Bodet, A. Lacointe, H. Cochard, Winter embolism, mechanisms of xylem hydraulic conductivity recovery and springtime growth patterns in walnut and peach trees, Tree Physiol. 22 (2002) 1211–1220, https://doi.org/10.1093/treephys/22.17.1211.
[39] H. Cochard, D. Lemoine, T. Améglio, A. Granier, Mechanisms of xylem recovery from winter embolism in Fagus sylvatica, Tree Physiol. 21 (2001) 27–33, https://doi.org/10.1093/treephys/21.1.27.
[40] J. Urban, E. Bednarova, R. Plichta, V. Gryc, H. Vavrčík, J. Hacura, M. Fajstavr, J. Kučera, Links between phenology and ecophysiology in a European beech forest, iForest-Biogeosciences and Forestry 8 (2014) 438. https://doi.org/10.3832/ifor1307-007.
[41] J.J. Sauter, B. van Cleve, Storage, mobilization and interrelations of starch, sugars, protein and fat in the ray storage tissue of poplar trees, Trees 8 (1994) 297–304, https://doi.org/10.1007/BF00202674.
[42] S. Pfautsch, Hydraulic anatomy and function of trees—basics and critical developments, Curr. Forest. Rep. 2 (2016) 236–248, https://doi.org/10.1007/s40725-016-0046-8.
[43] A.J.E. van BEL, Xylem-phloem exchange via the rays: the undervalued route of transport, J. Exp. Bot. 41 (1990) 631–644, https://doi.org/10.1093/jxb/41.6.631.
[44] M.J. Clearwater, G. Goldstein, N.M. Holbrook, M.A. Zwieniecki, Vascular transport in plants, Academic Press, Burlington, 2005, pp. 375–399.
[45] P. Copini, F.J. Vergeldt, P. Fonti, U. Sass-Klaassen, J. den Ouden, F. Sterck, M. Decuyper, E. Gerkema, C.W. Windt, H. van As, Magnetic resonance imaging suggests functional role of previous year vessels and fibres in ring-porous sap flow resumption, Tree Physiol. 39 (2019) 1009–1018, https://doi.org/10.1093/treephys/tpz019.
[46] U. Hacke (Ed.), Functional and ecological xylem anatomy, Springer, Cham, 2015.